"Understanding Optical Properties and Electronic Structures of High-Entropy Alloyed Perovskite Nanocrystals"

Yung-Tai Chiang[a]#, Sunil B. Shivarudraiah[a]#, Alexander Wieczorek[b], Khoong Hong Khoo[c], Zhidong Leong[c], Jia Wei Melvin Lim[d], Zengshan Xing[d], Sudhir Kumar[a], Simon F. Solari[a], Yen-Ting Li[e],[f], Yu-Cheng Chiu[e],[g], Tze Chien Sum[d]*, Yun Liu[c]*, Sebastian Siol[b]*, Chih-Jen Shih[a]*

[a] Institute for Chemical and Bioengineering, ETH Zürich, 8093 Zürich, Switzerland
E-mail: chih-jen.shih@chem.ethz.ch

[b] Laboratory for Surface Science and Coating Technologies, Empa – Swiss Federal Laboratories for Materials Science and Technology, 8600 Dübendorf, Switzerland
E-mail: sebastian.siol@empa.ch

[c] Institute of High Performance Computing (IHPC), Agency for Science, Technology and Research (A*STAR),1 Fusionopolis Way, 16-16 Connexis, Singapore 138632, Republic of Singapore
E-mail: liu_yun@ihpc.a-star.edu.sg

[d] Division of Physics and Applied Physics, School of Physical and Mathematical Sciences, Nanyang Technological University, 21 Nanyang Link, Singapore 637371, Singapore
E-mail: tzechien@ntu.edu.sg

[e] Department of Chemical Engineering, National Taiwan University of Science and Technology, Taipei 10607, Taiwan

[f] National Synchrotron Radiation Research Center, Hsinchu 30076, Taiwan

[g] Advanced Research Center for Green Materials Science and Technology, National Taiwan University, Taipei 10617, Taiwan

# These authors contribute equally.

Abstract: High-entropy alloying (HEA) has emerged as a prominent strategy to modulate physiochemical properties of nanomaterials. Nevertheless, this approach is underexplored in luminescent semiconductor nanocrystals (NCs) due to the lack of understanding into the HEA-induced electronic effect and photophysical behaviors. Herein, harnessing the defect tolerance of metal halide perovskite NCs, we systematically synthesized and characterized high-entropy halide perovskite (HEP) NCs containing multiple B-site elements (Pb^{2+}, Sr^{2+}, Ca^{2+}, Cd^{2+}, and Mg^{2+}). High-resolution transmission electron microscopy, transient photoluminescence and absorption spectroscopy, X-ray photoemission spectroscopy, and density functional theory simulations are employed to unravel the evolution of electronic structures with respect to alloying degree and link them to the spectral signatures and photostability. Counterintuitively, although the HEP NCs exhibit lateral sizes smaller than the Bohr diameter, HEA reduces the band dispersion and broadens the conduction band, thereby vanishing the excitonic feature by forming near band-edge shallow states. We show that these HEA-induced shallow states foster rapid radiative recombination and improve photostability, accompanied by a significantly reduced lead content by up to 70%. These findings pioneer understanding of the correlation between HEA-induced electronic effect and photophysical properties, highlighting the versatility of HEA for band structure engineering and stabilization of metal halide perovskites NCs.

Introduction

The discovery of multi-component alloys has generated considerable research interests across various material systems, including ceramics, semiconductor oxides, and metals owing to the extensive compositional space and unique functionalities derived from the large configurational entropy.[1-4] The incorporation of more than four primary and secondary elements into a single-phase solid solution is able to unlock new physiochemical properties, such as exceptional thermal stability, improved wear resistance, and unique electronic features, rendering them attractive for aerospace, automotive, energy, and catalysis applications.[5-9] Analogous to bulk high-entropy alloys, which typically require high-temperature synthesis, high-entropy nanoparticles have also showcased promising

results by exploiting colloidal ligand chemistry and different coordinating solvents.[10-12] Although phase segregation is generally thermodynamically favorable, efficient strategies such as configuration of elements, precise composition control, and judicious selection of surfactants, are capable of stabilizing high-entropy nanoparticles at metastable states.[13-15] Accordingly, several high-entropy nanoparticle systems have been reported, for instance intermetallics,[16-17] metal sulfides,[18-19] metal oxides,[20] and metal oxysulfides.[21] Nevertheless, there are limited reports deploying the high-entropy concept in fluorescent colloidal nanocrystals (NCs) for optoelectronic applications, likely because the extensive alloying process introduces crystalline defects and suppresses efficient excitonic recombination, thereby lowering the quantum efficiency.[22-23]

In this regard, the advancement of lead halide perovskite (LHP) NCs enlightens a new framework for HEA owing to the intrinsic defect tolerance nature and high photoluminescence quantum yields (η_{PL}).[24-27] Theoretically, the incorporation of multiple elements could be achieved by substituting the B-site atom with multiple divalent ions in the perovskite ABX_3 crystal lattice. Indeed, although the partial replacement of B-site Pb^{2+} ions by one or two metal cations has been extensively investigated, with primary efforts dedicated to uncover the roles of surface defects[28-31] and trap states,[32-35] fundamental understanding of B-site HEA effect and their link to photophysical properties still remains elusive. Since the electronic structure is dictated by the B-site valence shells, it is expected that the change in orbital hybridization will modulate the effective mass of excitons and induce lattice symmetry breaking.[36-37] Previously, we reported a solid-phase synthesis protocol for the preparation of HEP NCs based on methylammonium lead bromide ($MAPbBr_3$) NCs, leading to a substantial reduction of lead content by up to 55% and near-unity η_{PL}.[38] Similarly, HEA-based perovskite NCs were synthesized via a rapid room-temperature process,[39] and optimized to achieve highly efficient and spectrally stable electroluminescence.[40] Despite significant progresses, it remains unclear that how HEA rectifies the electronic structure of LHP NCs and modulate their excitonic behaviors, which is crucial to unlock their full potential and realize advanced optoelectronic applications. Herein, combining high-resolution transmission electron microscopy, transient photoluminescence and absorption spectroscopy, X-ray photoemission spectroscopy, and density functional theory simulations, we narrow the gap between the understanding of electronic structures and novel optical properties of HEP NCs.

Results and Discussion

STRUCTURAL AND OPTICAL CHARACTERISTICS OF HEP NCS

B-site HEP NCs were systematically prepared through ligand-assisted multi-cationic exchange of $CsPbBr_3$ NCs. In brief, $CsPbBr_3$ NCs were first synthesized using a ligand-assisted reprecipitation protocol.[41] Subsequently, the colloidal solutions were mixed with excess divalent metal bromide salts (MBr_2, where M^{2+} = Sr^{2+}, Ca^{2+}, Cd^{2+}, Mg^{2+}) partially dissolved in nonpolar toluene via the addition of amphiphilic ligands (details see **Supplementary Section 1.2**). Due to the soft ionic lattice nature of lead halide perovskites, the partial and gradual substitution of Pb^{2+} with ligand-stabilized M^{2+} gradually became entropically favorable,[31] thus forming the B-site HEP NCs. **Figure 1a** presents a schematic diagram illustrating a HEP NC containing approximately 1000 $[MBr_6]^{4-}$ octahedral unit cells, in which M^{2+} ions are embedded in the lattice through HEA. For each colloidal NC sample synthesized, we prepared sold thin films by drop-casting the solution onto silicon substrates, followed by extensive energy-dispersive X-ray spectroscopy (EDS) in a scanning electron microscope (SEM) or on TEM grids using high-resolution (HR) scanning transmission electron microscopy (STEM) (**Figure S1-S5** and **Table S1)**. **Figure 1b** shows a representative HRSTEM EDS mapping result for $Cs(PbSrCdMg)Br_3$ HEP NCs, highlighting the alloying elements, Mg, Cd, and Sr, are randomly distributed within individual NC, without phase separation or metal segregation.

Our systematic SEM EDS measurements enable quantitative estimation of atomic ratios Cs:Br and (Pb+M):M for all synthesized samples (**Figure 1c, Figure S6-S8,** and **Table S2**). The Cs:Br ratio nicely aligns with the expected perovskite stoichiometry of 3, showing that our synthetic protocol did not alter the A-site composition significantly. Alternatively, despite a degree of variation, there exists a clear trend that the (Pb+M):M ratio increases substantially with more secondary elements, which is driven by the increasing configurational entropy of the systems. For simplification, the B-site elements are used to denote each HEP NC synthesized in this work. We discovered that the majority of secondary M^{2+} ions, especially the smaller Cd^{2+} and Mg^{2+} ions, replaced the B-site Pb^{2+} ions, which aligns with the substitutional mechanism proposed by Phung et al. in monodoped perovskite NCs.[42] Importantly, our results indicate that the toxic Pb^{2+} could be effectively reduced by up to 70% using our protocol, rendering the commercial applications of the HEP NCs much more attractive.

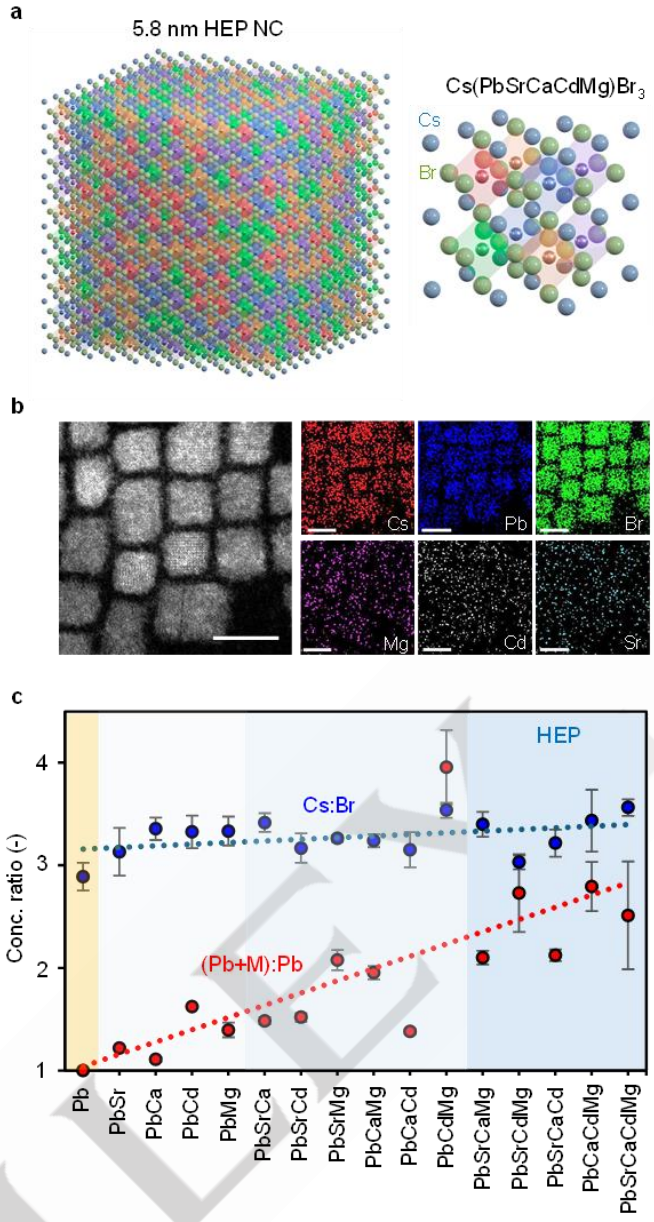

Figure 1. Concept of HEP NCs. (a) Schematic illustration of a B-site HEP NC containing approximately 1000 $[MBr_6]^{4-}$ octahedral unit cells. (b) Representative HRSTEM EDS map for $Cs(PbSrCdMg)Br_3$ HEP NCs, revealing that the alloying elements, Mg, Cd, and Sr, are randomly distributed within individual NCs. Scale bars: 5 nm. (c) Statistical analysis for the EDS-analyzed Cs:Br and (Pb+M):Pb ratios for all NC samples considered in this study. The toxic Pb^{2+} could be largely reduced by up to 70% using our HEP protocol.

We examined the structural and crystallographic properties of HEP NCs (**Figure 2**). High-resolution scanning transmission electron microscopy (HRSTEM) is used to analyze and quantify the crystallographic profiles of parent $CsPbBr_3$ and three representative HEP NCs, including $Cs(PbSrCdMg)Br_3$, $Cs(PbCaCdMg)Br_3$, and $Cs(PbSrCaCdMg)Br_3$ (**Figure 2 a** and **b**). The atomically resolved images allow us to precisely quantify the lattice parameter *d*-spacing, |*a*|, exhibiting a reduction from 5.89 to 5.81 Å upon HEA. These findings agree well with the smaller ionic radii of the doping cations compared to Pb^{2+}. We did not observe phase separation within individual HEP NC, echoing the previous EDS results. The corresponding X-ray diffraction (XRD) crystallographs suggest that all the synthesized HEP NCs inherit the parent orthorhombic structure (**Figure S9-S10**), with a slight degree of lattice contraction consistent with the HRSTEM observation. Interestingly, upon HEA, in addition to lattice contraction, statistical TEM analysis revealed that the lateral size of the synthesized NCs substantially decreased from 10 nm to approximately 5.5 nm for the quaternary and quinary HEP NCs, while possessing high monodispersity (**Figure 2c** and **S11**). We attribute the observed NC size reduction to: (i) the addition of excess ligands in the synthetic protocol, and (ii) re-assembly of M-site octahedral unit cells.[31, 43-44] We would like to point

out that the average size for the quaternary and quinary HEP NCs are all below 6 nm, considerably smaller than the Bohr diameter (d_B) of $CsPbBr_3$ (~7 nm).[45]

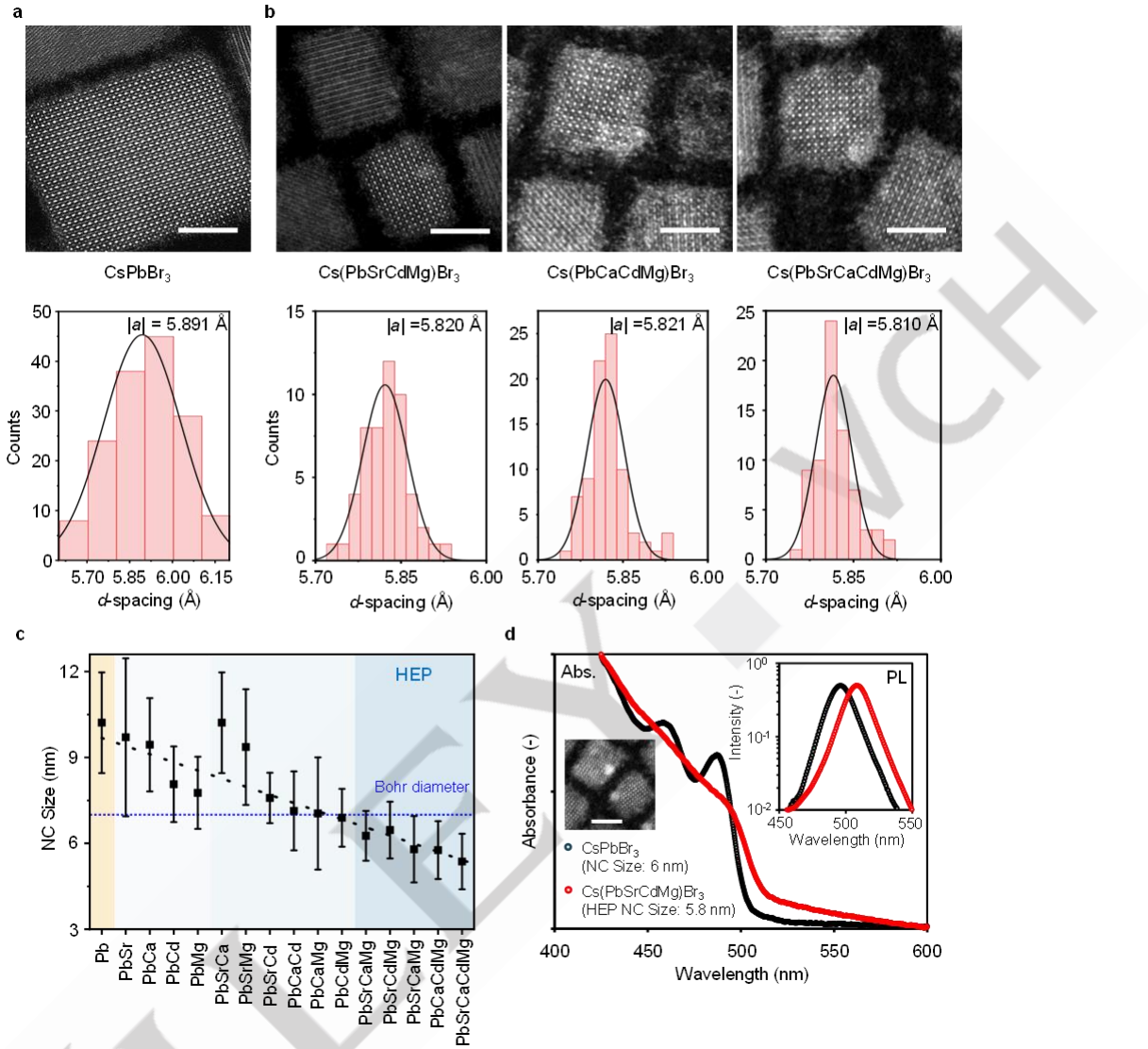

Figure 2. Structural and crystallographic properties of HEP NCs. (a,b) HRSTEM images (top) and extracted lattice parameters (bottom) for (a) the parent $CsPbBr_3$ and (b) HEP NCs. Upon HEA, the perovskite lattice contracts resulting from doping of small-radii B-site M^{2+} ions. Scale bars: 5 nm. (c) Statistical analysis for the NC lateral sizes extracted from the TEM images of synthesized NCs, showing a reduction of size. In particular, HEP NCs of B-site alloying of more than three extra ions decreases the size below the Bohr diameter of $CsPbBr_3$ (~ 7 nm). (d) Comparison of absorption (Abs.) and photoluminescence (PL; right inset) spectra for HEP (average NC size: 5.7 nm; red curves) and quantum-confined $CsPbBr_3$ (average NC size: ~ 6 nm; black curves) NCs, showing a lack of excitonic feature for HEP NCs. Left inset: HRSTEM image for the quantum-confined $CsPbBr_3$ NCs. Scale bar: 5 nm.

Optical characterizations are then employed to investigate the steady state absorption and emission spectra for the colloidal HEP NCs (**Figure S12-S14**). Surprisingly, although the small NC sizes should give rise to a strong quantum-confined nature, all absorption spectra lack excitonic feature and showcase a smooth bandgap edge. For comparison, we synthesized the quantum-confined $CsPbBr_3$ NCs with an average NC size of ~6 nm (HRSTEM image see **Figure 2d** inset). **Figure 2d** compares the absorption spectra between the 5.7 nm $Cs(PbSrCdMg)Br_3$ HEP and the 6 nm $CsPbBr_3$ NCs. Clearly, in addition to the lack of discernable features of confined resonance, the $Cs(PbSrCdMg)Br_3$ HEP NCs exhibit a smaller hypsochromic shift (the emission wavelength $\boldsymbol{\lambda_{PL} = 506}$ nm). Furthermore, the long-tail absorption at the band edge, together with the slightly stoke-shifted photoemission, suggest the presence of shallow states upon HEA.[46-48] We noticed that these optical behaviors are in stark contrast with the quantum-confined $CsPbBr_3$ NCs, where a larger bandgap along with a strong absorption peak locating at 475 nm are present due to the quantized density of states (DOS).[49] Note that we had confirmed the extended absorption tail does not result from the optical scattering effects, as we filtered the colloidal solution through a

porous 0.2 μm Polytetrafluoroethylene (PTFE) filter and excited the solution at the tail wavelength region (**Figure S15**). Our findings clearly indicate that the electronic configuration of the small HEP NCs behave closer to bulk semiconductors rather than confined quantum dots (QDs); in other words, the classical quantum confinement fails to describe the unique photoelectronic properties of HEP NCs. Detailed characterizations are then performed to unravel the mechanisms governing the anomalous optical behaviors.

SHALLOW STATES-ASSISTED RAPID PHOTOEMISSION

Figure 3 presents the photophysical properties of HEP NCs. Compared to the parent $CsPbBr_3$ NCs, the solution and thin-film η_{PL} are substantially enhanced in alloyed NCs, attaining the highest values for $Cs(PbCaMg)Br_3$ NCs (~90% and ~100% for thin films and solutions, respectively; see **Figure 3a**). Nevertheless, for HEP NCs, the solution PL quenches slightly in the quaternary and quinary B-site systems, presumably owing to trap states introduced by extensive alloying.[50] Interestingly, the HEP NC thin-film samples universally attain high η_{PL} of >90%, which is attributed to the ligand adsorption/desorption equilibrium and NC self-assembly minimizing the non-radiative pathways[51] and the aggregation-induced emission due to restricted motion of surface ligands.[52] The is confirmed qualitatively by close inspection of the SEM images and quantitatively by grazing incident small-angle X-ray diffraction of HEP NC films, showcasing the formation of self-assembled cubic superlattices that fosters long-range packing and reducing the number of undercoordinated bonds (**Figures S16-S17**).[53] Hereafter, the photophysical characterization is based the thin-film samples. The boosted radiative recombination efficiency in HEP NCs reaffirms a distinct emission mechanism from quantum-confined NCs, where a significantly low η_{PL} are observed (η_{PL}=30%).[45, 54]

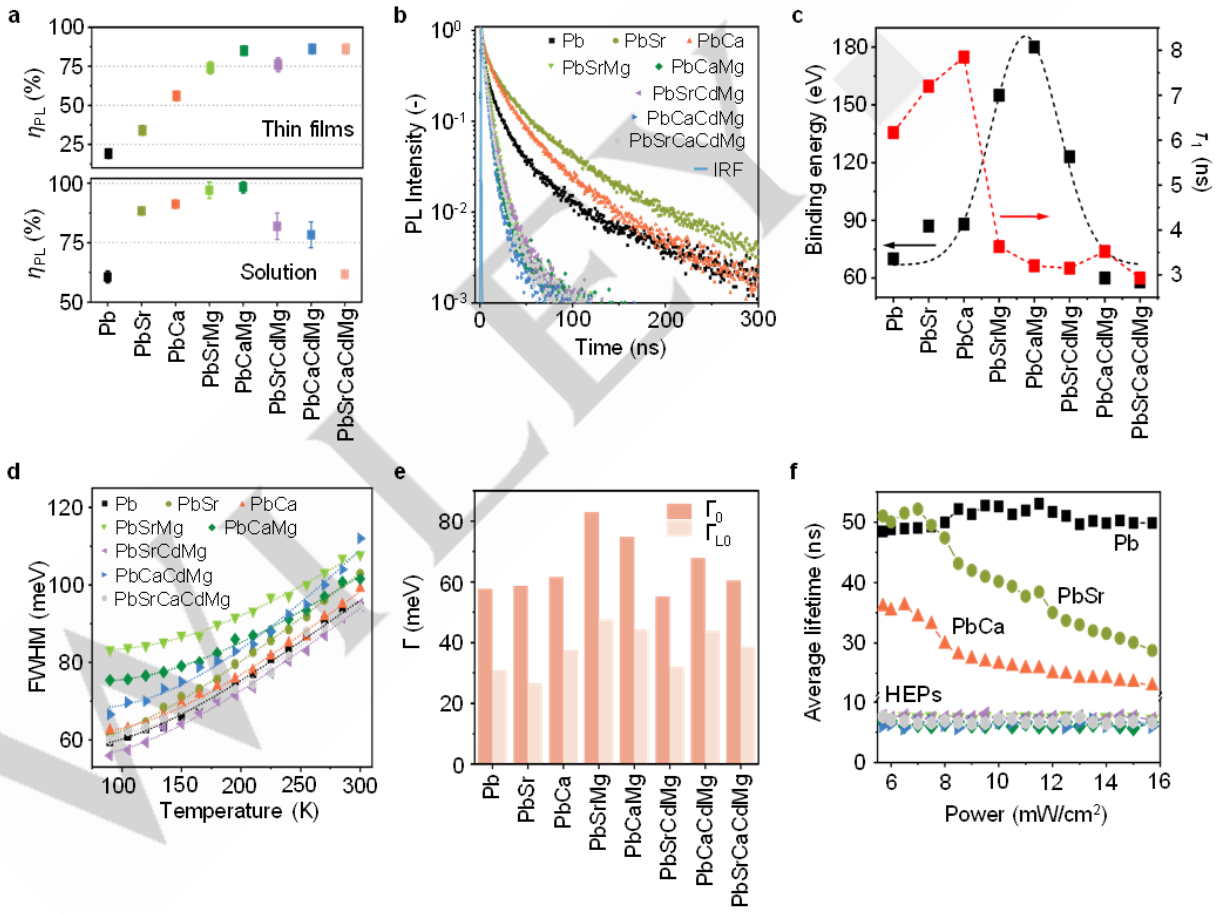

Figure 3. Photophysical characterization of HEP NCs. Room-temperature (**a**) solution and thin-film η_{PL} and (**b**) TRPL responses for HEP NCs. (**c**) The exciton binding energy extracted from variable temperature PL measurements and the prompt radiative lifetime component τ_1 characterized at room temperature. (**d**) The variation of emission FWHM values characterized at low temperatures. (**e**) The extracted peak broadening contributions from lattice imperfection (Γ_0) and longitudinal phonon scattering (Γ_{LO}) by fitting with the Fröhlich equation. (**f**) Extracted exciton lifetimes at room temperature with respect to excitation power for the HEP NCs.

To unravel the carrier recombination dynamics in HEP NCs, we performed room-temperature time-resolved (TR) PL spectroscopy of HEP NCs thin films (**Figure 3b**). Interestingly, according to the enhanced η_{PL} relative to parent $CsPbBr_3$ NCs, one might anticipate elongated lifetimes induced by defect or surface passivation.[55-58] However, in all HEP NC species considered here, the average PL lifetime significantly decreased by up to nearly one order of magnitude, from 48.4 ns to as low as 6.1 ns upon HEA (**Table S3**). A similar PL lifetime reduction is also observed in the quantum-confined $CsPbBr_3$ NCs, suggesting that size effect cannot be ignored (**Figure S18** and **Table S3**). To explore different radiative channels and their contributions, we examined the TRPL decay at cryogenic temperatures between 77 to 300 K, in which the trap states are mitigated to allow the intrinsic recombination process to dominate.[59-60] Each TRPL response was fitted with a bi- or tri-exponential function, where the most rapid component conforms to the band-edge radiative recombination at low temperatures, while the second and third components can be assigned to shallow and deep trap-assisted recombination, respectively.[61-62] Surprisingly, the average PL lifetimes of HEP NCs are reduced by a factor of 18 when the temperature decreases from 300 to 77 K (**Figure S19** and **Table S4**), whereas that for parent $CsPbBr_3$ and single-doped NCs only decreased by two folds. Because the defects- / deep-states-mediated pathways are quenched at low temperatures, the significant lifetime reduction in HEP NCs indicates that the band-edge- and shallow-states-mediated radiative recombination are substantially accelerated. We can therefore infer that the shallow states introduced in HEA are responsible for the rapid photon emission observed here.[63-64]

To further strengthen our hypothesis, temperature-dependent PL intensities are analyzed (**Figures S20**-**S22**), allowing us to extract the exciton binding energy using the Arrhenius equation.[65-67] We found that trinary perovskite NCs, such as $Cs(PbCaMg)Br_3$, yield the highest binding energy up to 180 meV, as compared to 70 meV in parent $CsPbBr_3$ NCs (**Figure 3c**). Remarkably, this exceptionally high binding energy is typically found only in strongly confined nanocrystals.[68] As the trinary NC sizes remain larger than the Bohr diameter (see **Figure 2c**), and the absorption spectra lack the excitonic feature (see **Figure S12**), we attribute the enhanced band-edge recombination to the high binding energy, endorsing the extremely short prompt radiative lifetime value at room temperature (~3 ns). However, excessive alloying in HEP NC systems reverses the trend, decreasing the binding energy, despite the confinement effects resulting from the NC size reduction (**Figure 2c**). We hypothesize that excessive alloying induces wavefunction delocalization that disrupts the recombination process. This highlights the concomitant existence of strong exciton localization induced by size reduction and HEA in HEP NCs.[69-70]

Indeed, our synthesized HEP NCs are not "defect-free". We characterized the PL full width at half maximum (FWHM) at various temperatures and fitted with the Fröhlich equation (**Figures 3d** and **3e**).[71] The relatively higher values for the extracted peak broadening contribution from lattice imperfection, Γ_0, suggest the increase of defective sites upon HEA. To further elucidate the role of defects, **Figure 3f** compares the extracted average radiative lifetimes with respect to the pumping laser power. Among the NC samples considered here, two distinct trends were identified: lifetimes of parent $CsPbBr_3$ NCs remained approximately constant and independent of the laser power, while those for binary alloyed NCs decrease with increasing laser power. The lifetime decreases at high laser powers, according to previous reports,[72] result from the populated trapped states that promote the bimolecular exciton-exciton annihilation at high laser powers. In HEP NCs, however, this effect appears to be counter-balanced, exhibiting power-independent lifetimes (**Figure 3f**). Echoing the observed binding energy decrease in HEP NCs (**Figure 3c**), the exciton localization and suppressed diffusion may suppress the many-body recombination processes upon HEA.[73-74]

We further investigated the non-radiative charge carrier dynamics of HEP NCs using the transient absorption (TA) spectroscopy. **Figures 4a** and **4b** show the representative TA spectra for the parent $CsPbBr_3$ and $Cs(PbSrCdMg)Br_3$ HEP NCs in solutions, exhibiting a dominant positive signal corresponding to the ground state bleaching (GSB) at the band edge wavelengths of 516 and 507 nm, respectively. **Figure 4c** compares the GSB kinetics that characterize the excited-state carrier dynamics for a number of NC samples considered here. Overall, the samples with higher numbers of alloying elements exhibit shorter carrier lifetimes. The GSB kinetics were further probed at various pumping powers (**Figures 4d and 4e**, and **Figure S23**), followed by globally fitting with the triexponential functions with the instrument response function deconvolved (**Figure 4f** and **Table S5**). The kinetics at low fluence demonstrates a mono-exponential decay, characterizing the exciton lifetime τ_1. In contrast, the τ_2 and τ_3 appear at higher pump fluences, attributed to the multiexciton processes of biexcitons and trions, respectively.[75] The obtained lifetimes of biexcitons (tens of picosecond) and trions (hundreds of picosecond) are in line with their reported time scales in halide perovskite NCs. [75-77]

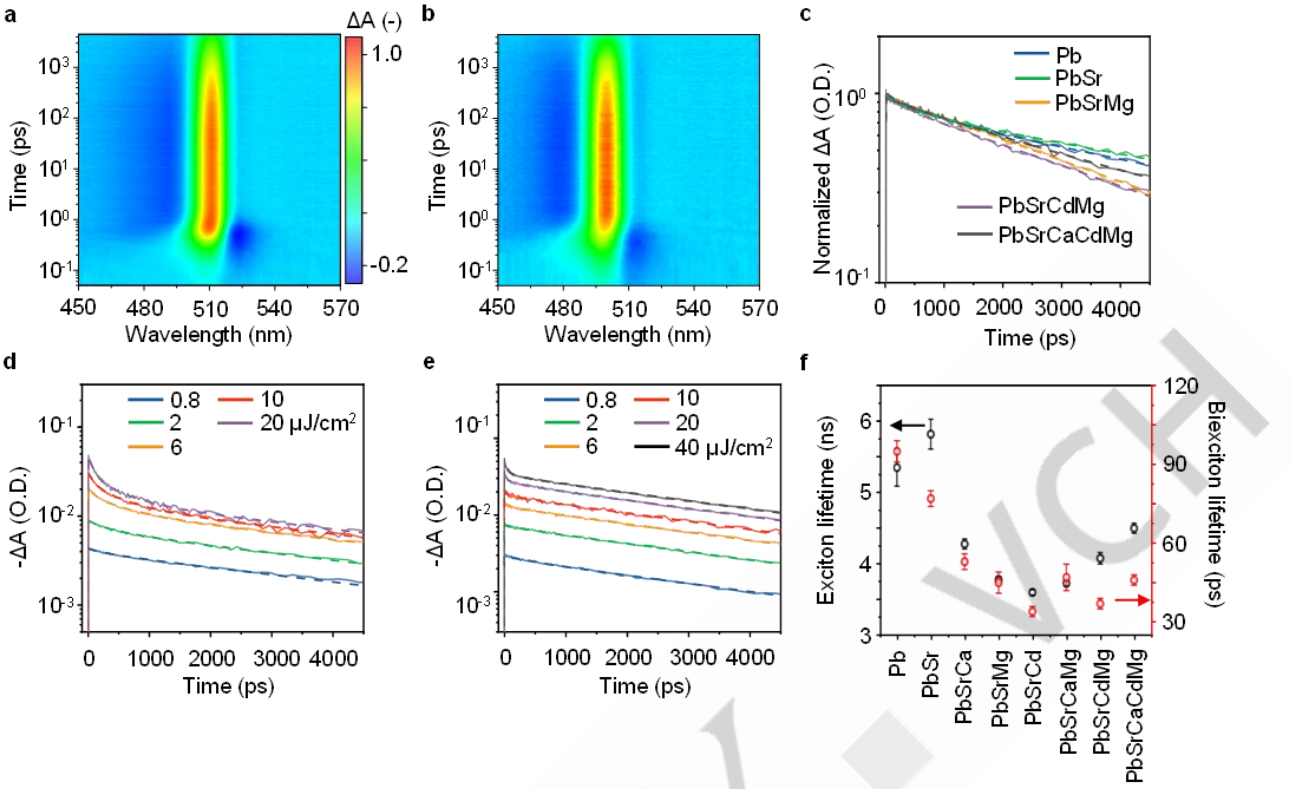

Figure 4. Transient absorption (TA) responses of HEP NCs. Representative TA spectra for (a) parent $CsPbBr_3$ and (b) $Cs(PbSrCdMg)Br_3$ NCs excited at 400 nm. (c) Comparison of GSB kinetics for NC samples with different doping elements at low pump fluence of ~0.8μJ/cm^2. Pump power-dependent GSB kinetics for (d) $CsPbBr_3$ and (e) $Cs(PbSrCdMg)Br_3$ NCs. The dashed curves correspond to fittings of tri-exponential functions convoluted with instrument response function. (f) Extracted exciton and biexciton lifetimes from the pump power-dependent GSB kinetics.

Overall, the exciton and biexciton lifetimes become shorter upon metal alloying. Although one could attribute the observation to the NC size reduction in HEP NCs (**Figure 2c** and **Figure S24**), we noticed that the trends for exciton and biexciton lifetimes upon alloying with multiple metal elements are different, highlighting the role of alloying apart from the size effect. Specifically, as shown in **Figure 4f**, the biexciton lifetimes for trinary, quaternary, and quinary metal NCs are nearly identical, irrespective of the NC size. On the contrary, the exciton lifetimes reach a minimum in the trinary NCs. Despite very small NC sizes for HEP NCs, the exciton lifetimes increase again upon HEA, consistent with the trend in exciton binding energy (**Figure 3c**). We therefore conclude that the exciton binding energy underpins the observed exciton kinetics.

COMPUTATIONAL INSIGHT INTO THE ELECTRONIC STRUCTURE

We carried out the density functional theory (DFT) simulations to elucidate the electronic structures of HEPs. We considered representative trinary, quaternary, and quinary systems with B-site elemental compositions given by the experimental characterizations of $Cs(PbSrMg)Br_3$, $Cs(PbSrCdMg)Br_3$, and $Cs(PbSrCaCdMg)Br_3$ NCs. For tractable computations, we constructed special quasi-random structures with 360-atom supercells which approximate the disordered arrangement of B-site atoms. **Figure 5** presents the calculated electronic structures.[78] The valence band maximum (VBM) in HEPs is predominantly composed of Br with some contribution from Pb, while the conduction band minimum (CBM) is primarily dominated by Pb with a smaller contribution from Br, resembling the $CsPbBr_3$ system.[79] In the four- and five-component systems containing Cd, there is also significant Cd *p*-like character at the CBM. Other elements contribute marginally to the band edge states; most states are energetically far away from the band gap. We note that the Cd dominated CBM states are separated energetically from the continuous conduction bands by about 0.1 eV, which might correspond to shallow trap states observed in the TRPL responses.

For quaternary and quinary HEPs, the calculated band structures (**Figures 5b** and **5c**) reveal that they are indirect band gap semiconductors with the VBM and CBM located away from Γ-point. These HEP systems having a large

degree of Pb replacement also exhibit relatively flat and non-dispersive bands. In contrast, for the trinary system with a relatively higher Pb content, the direct band gap is located at the Γ-point with a much more dispersive band edge states, similar to pure $CsPbBr_3$ NCs.[80] **Figure S25a** compares the DFT calculated bandgap values, suggesting that HEA results in a drastic bandgap widening. This increase in bandgap has been reported in other doped perovskite nanocrystals,[81] which is attributed to the crystal symmetry breaking from the bonding and anti-bonding orbitals in perovskites.[82] Interestingly, as the degree of alloying increases, the calculated bandgap values remain approximately constant within the narrow energy range, in agreement with our experimental photophysical measurements.

We further extracted the electron and hole effective masses by parabolic fitting of the band edge states (**Figure S25b**), revealing a gradual increase of the effective masses with decreasing the Pb content. It underlies the increasingly non-dispersive nature of band structure upon HEA, as the presence of Pb yields stronger covalent interactions in the system, leading to more dispersive bands. The increase of effective mass also contributes to a smaller excitonic radius, leading to faster radiative recombination rates and shorter radiative lifetimes,[82-83] consistent with our experimental observations, as illustrated in **Figures 2** to **4**.

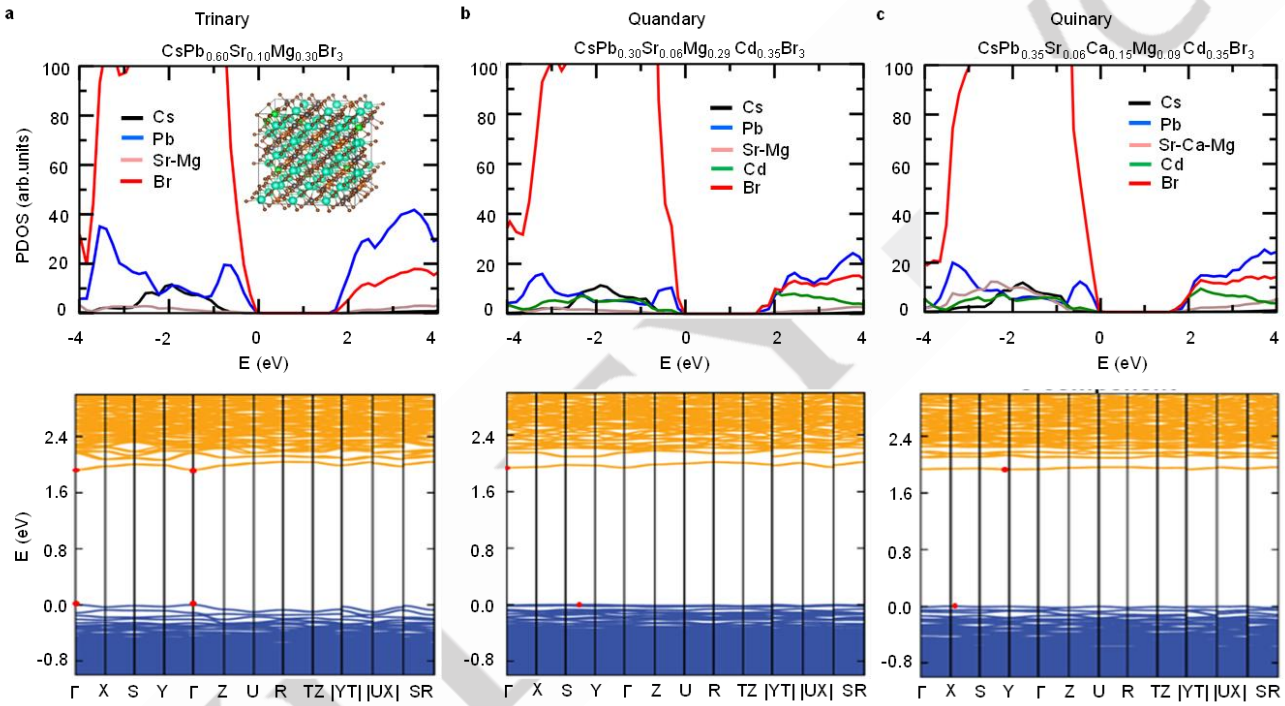

Figure 5. Calculated electronic band structures of HEP systems. DFT-calculated projected density of states (PDOS; top row) and corresponding electronic band structures along high symmetry directions (bottom row) for representative (a) trinary $Cs(PbSrMg)Br_3$, (b) quaternary $Cs(PbSrMgCd)Br_3$, and (c) quinary $Cs(PbSrCaMgCd)Br_3$. The valence and conduction bands correspond to blue and orange curves, respectively, and red points highlight the band minima / maxima. The inset shows a representative trinary supercell in DFT calculations.

ELECTRONIC BAND DISPERSION IN HEP NCS

To further elucidate the electronic structures of HEP NCs experimentally, we carried out X-ray photoelectron spectroscopy (XPS), which directly informs the density of states at the valence band edge (**Figure 6a**). While the parent $CsPbBr_3$ NCs exhibits sharp valence states, we observed an increased dispersion for the valence band states upon alloying. In particular, for quaternary and quinary HEP NCs, the spectra reveal featureless and broad distribution of states, in agreement with the DFT simulation results discussed earlier. Analogous to recent findings in high-entropy nanoparticle catalysts,[84] the valence band dispersion results from the hybridization of states within the B-site elements incorporated into the perovskite lattices. The findings nicely explain the observed extended Urbach tails in absorption spectra upon HEA (**Figure 2d** and **Figure S12**).

We further analyzed the chemical states extracted from the core level spectra. The Cs 3d, Br 3p, and Pb 4f features remain highly symmetric for each metal-doped NC sample **(Figures S26-40**), indicating the presence of a single dominant chemical state for each individual element. Notably, for XPS analysis of semiconductors and insulators,

the charging effects may induce shifts in the spectra on the energy scale.[85] Although charge referencing based on adventitious carbon is often applied to counter this effect, insufficient electrical contact of the adsorbate layer to the investigated sample could induce uncertainties of up to 2 eV.[86] To circumvent these issues, internal charge referencing has recently been established as a technique to perform precise XPS analysis for semiconductors,[87-90] where the relative distance of two features inherent to the investigated samples are compared. Similar to our recently reported $CsPbI_3$ nanoplatelets,[91] we extracted the relative distance (ΔE_b) between the Pb-site (Pb $4f_{7/2}$) and halide-site (Br $3p_{5/2}$) peaks to qualitatively analyze the local chemical environment of the Pb-site, as schematically illustrated in **Figure 5b**.

Applying this concept on each sample considered here yields a clear correlation of the Pb chemical state in relation to its attenuation relative to the Br 3p peak (**Figure 5c**). With increasing alloying of the B-site element, a continuous change of its chemical state is observed. The relative increase of the binding energies by up to 0.2 eV suggests an increased electron density at the Pb-site relative to the Br reference. Strikingly, this trend is not governed by the type of metal incorporated into the lattice, despite their variable electronegativity. This may suggest that the structural change induced upon alloying, such as the octahedral contraction previously observed from the structural analysis (**Figures 2a** and **b**), dominates change in the Pb–Br bonding. Interestingly, $Cs(PbSrMg)Br_3$ and its quaternary derivative $Cs(PbSrCaMg)Br_3$ exhibited a chemical state that did not fall into this overall trend. This may result from the formation of structural defects on the NC surface for these samples and/or the lower suitability of these dopants for our synthetic protocol.

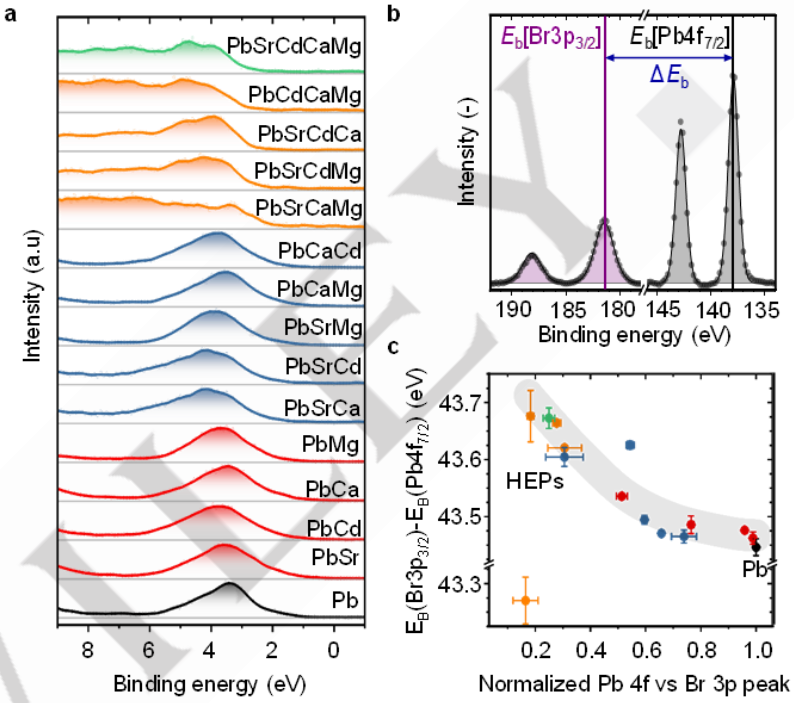

Figure 6. XPS characterization revealing electronic structures of HEP NCs. (a) Low-energy XPS spectra for parent CsPbBr3 (Pb) and all B-site doped NC samples resolving the density of states at the conduction band edge. (b) Concept of relative binding energies for robust semiconductor surface analysis. (c) Correlation of Pb 4f peak area attenuation versus Br 3p reference against the relative binding energy.

ENHANCED PHOTOSTABILITY IN HEP NCS

Photostability of luminescent semiconductor nanocrystals has been recognized as the key consideration towards advanced optoelectronic applications.[92-93] We have examined the environmental stability of the HEP NCs considered here by *in-situ* monitoring the thin-film PL loss (**Figure 7** and **S41**), without any encapsulation. Taking advantage of an automated platform for optical stability assessment,[94] we were able to resolve the often non-linear changes with high temporal resolution over 96 h. As a benchmark, the $CsPbBr_3$ thin-film sample retained 68% of its initial PL intensity within the timeframe. Among the quaternary and quinary HEP NCs, the least stable sample exhibited similar performance with $CsPbBr_3$, while the most stable sample substantially outperformed, preserving 95% of their initial PL intensity.

Interestingly, among the B-site alloyed samples considered here, those with substantially enhanced photostability all contain Cd^{2+}, whereas Mg^{2+} alloying generally showed lowered performance. Indeed, Mg^{2+} alloying without Cd^{2+} may promote decomposition of the perovskite phase on the surface, because among all divalent metal ions considered here, Mg^{2+} has the smallest Shannon ionic radius (72 pm);[95] hence with the largest difference compared to Pb^{2+} (119 pm).[95] The ionic radius for Pb^{2+} is the most ideal for the stabilization $CsPbBr_3$ perovskite phase according to the Goldschmidt factor.[96] On the contrary, the more similar ionic radius of Cd^{2+} (95 pm)[95] might alleviate the shortcomings; for example in the $Cs(PbCaCdMg)Br_3$ NC composition.

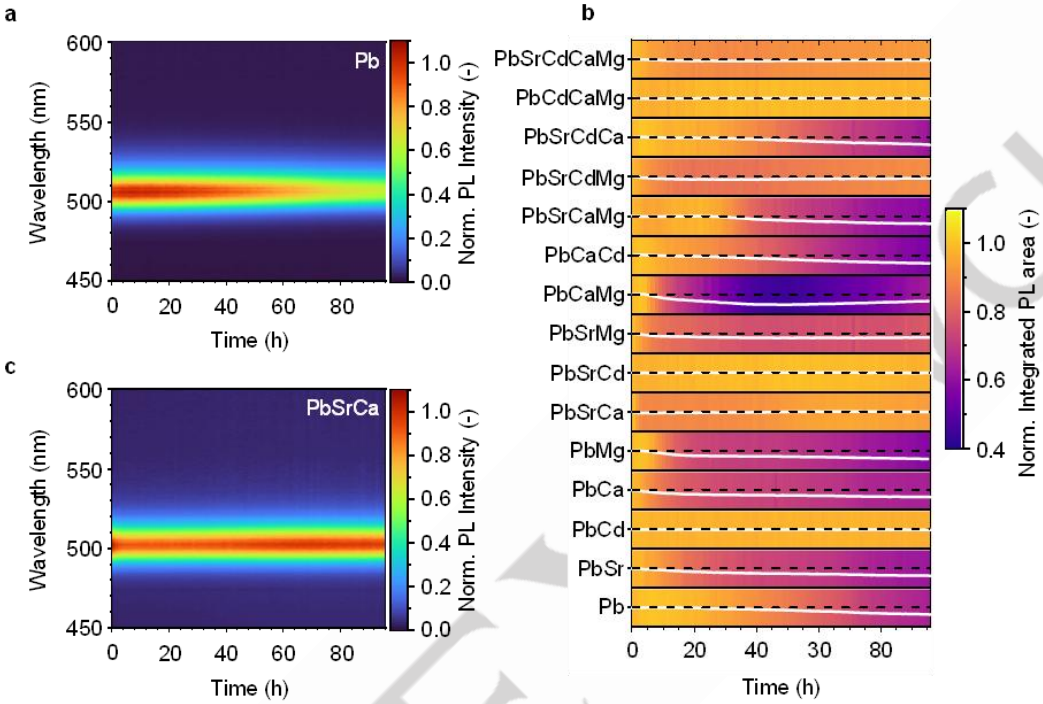

Figure 7. Enhanced photostability of metal-alloyed perovskite NCs. Spectral stability of in-situ PL aging for (a) CsPbBr3 benchmark and (b) trinary highly stable but reduced toxicity Cs(PbSrCa)Br3 samples, retaining 68% and 97% of their initial PL intensity, respectively, after 96 hours of continuous automated test. (c) Normalized integrated PL intensity with respect to time for all metal-doped perovskite NC samples considered in this study.

Remarkably, the systematic experimentation allowed us to identify a trinary B-site alloyed NC compound, $Cs(PbSrCa)Br_3$, showing extraordinary photostability but reduced toxicity by retaining (97±2)% of its initial PL intensity within 96-hour timeframe (**Figure 7c**). We consider this compound particularly attractive for commercial optoelectronic applications. At first glance, the ionic radii of Sr^{2+} (118 pm) and Ca^{2+} (100 pm) seem even more suitable for B-site alloying as compared to Cd^{2+}, but the binary $Cs(PbSr)Br_3$ and $Cs(PbCa)Br_3$ only showed similar stability with parent $CsPbBr_3$ NCs, retaining (61±3)% and (66.1±0.3)% of their initial PL intensities, respectively. The synergistic effect resulting from both suitable yet different ionic radii of Sr^{2+} and Ca^{2+} may offset local strains, thereby enhancing the PL stability. We notice that by alloying Sr^{2+}, the relatively low PL stability for $Cs(PbMg)Br_3$ (59.6±0.2%) was substantially enhanced (77.8±0.6%) for $Cs(PbSrMg)Br_3$. Consequently, the HEP NCs generally exhibit enhanced photostability compared to binary perovskite NCs. The complex interplay between different B-site alloying elements may motivate further in-depth investigations elucidating synthesis-structure-property relationships and data-driven compositional optimization.

Conclusion

In summary, we have synthesized a series of HEP NCs based on parent $CsPbBr_3$ perovskite system. The HEP NCs exhibit both enhanced η_{PL} and shortened PL lifetimes. Although the HEP NCs have NC size smaller than the Bohr diameter, their absorption spectra show the absence of confined resonance and the emergence of long-tail states, which cannot be explained using the classical quantum dot theory. Detailed temperature-dependent photophysical analyses reveal that B-site metal doping could increase the exciton binding energy and introduce shallow states near the band edge. The shallow states synergistically facilitate electron-hole radiative recombination with intrinsic band-edge photon emission. Our DFT simulations suggest that HEA reduces the band

dispersion, thereby resulting in higher effective electron and hole masses. The in-depth XPS measurement endorses the presence of shallow states and discloses gradual broadening of valence states with increasing degree of B-site alloying. The synthetic protocol presented here allows us to identify the HEP NC thin films with substantially enhanced photostability and reduced toxicity. Our findings uncover the fundamental mechanisms altering photophysical properties of HEP NCs, bridging the gap to correlate the electronic structure and B-site HEA. We believe that the data-driven optimization of compositional space for the development of next-generation luminescent quantum dots will be greatly facilitated by the fundamental principles and chemical methodology presented here.

Acknowledgements

The authors are grateful for ScopeM (ETH Zürich) for the access to electron microscopy. Y.T.C., S.B.S., A.W., S.K., S.S., and C.J.S. thank funding from the Strategic Focus Area–Advanced Manufacturing (SFA-AM) through the AMYS project and European Research Council (ERC) starting grant (N849229 - CQWLED). K. H. K., Z. L. and Y. L. acknowledge funding from A*STAR Young Achiever award and Career Development Fund (C233312001). Our computational resource is supported by the A*STAR Computational Resource Center (ACRC) and the National Supercomputing Centre (NSCC). T.C.S. J.W.M.L. and X.Z. acknowledge funding from the Ministry of Education under its AcRF Tier 2 grants (MOE-T2EP50120-0004 and MOE-T2EP50123-0001) and the National Research Foundation (NRF) Singapore under its Competitive Research Program (NRF-CRP25-2020-0004)

Author contribution

C.J.S. conceived the idea and coordinated the project; Y.T.C., S.B.S., and A.W. performed the majority of experiments and analyzed the data with input from S.K, S.S, Y.-T.L, Y.-C.C. and C.J.S.. Z.L. generated the SQS, and K.H.K. and Y.L. performed and supervised the DFT calculations, respectively. J.W.M.L. performed the TA experiments and analyzed data with Z.X., supervised by T.C.S. Y.T.C. and S.B.S. co-wrote the manuscript with input from A.W., Z.X., Y.L., S.K., S.F.S. and C.J.S. All authors commented on and approved the manuscript.

Keywords: High-entropy perovskites, shallow states, symmetry breaking, radiative lifetime

References

[1] Y. Yao, Q. Dong, A. Brozena, J. Luo, J. Miao, M. Chi, C. Wang, I. G. Kevrekidis, Z. J. Ren, J. Greeley, G. Wang, A. Anapolsky, L. Hu, *Science* **2022**, *376*, eabn3103.
[2] G. Pacchioni, *Nature Reviews Materials* **2022**, *7*, 156-156.
[3] W. Al Zoubi, R. A. K. Putri, M. R. Abukhadra, Y. G. Ko, *Nano Energy* **2023**, *110*, 108362.
[4] P.-C. Chen, M. Liu, J. S. Du, B. Meckes, S. Wang, H. Lin, V. P. Dravid, C. Wolverton, C. A. Mirkin, *Science* **2019**, *363*, 959-964.
[5] E. P. George, D. Raabe, R. O. Ritchie, *Nature Reviews Materials* **2019**, *4*, 515-534.
[6] C. Oses, C. Toher, S. Curtarolo, *Nature Reviews Materials* **2020**, *5*, 295-309.
[7] M. Fu, X. Ma, K. Zhao, X. Li, D. Su, *Iscience* **2021**, *24*.
[8] S. Schweidler, M. Botros, F. Strauss, Q. Wang, Y. Ma, L. Velasco, G. Cadilha Marques, A. Sarkar, C. Kübel, H. Hahn, J. Aghassi-Hagmann, T. Brezesinski, B. Breitung, *Nature Reviews Materials* **2024**, *9*, 266-281.
[9] Y. Sun, S. Dai, *Science Advances* **2021**, *7*, eabg1600.
[10] C. R. McCormick, R. E. Schaak, *Journal of the American Chemical Society* **2021**, *143*, 1017-1023.
[11] D. Wu, K. Kusada, T. Yamamoto, T. Toriyama, S. Matsumura, S. Kawaguchi, Y. Kubota, H. Kitagawa, *Journal of the American Chemical Society* **2020**, *142*, 13833-13838.
[12] B. Wang, C. Wang, X. Yu, Y. Cao, L. Gao, C. Wu, Y. Yao, Z. Lin, Z. Zou, *Nature Synthesis* **2022**, *1*, 138-146.
[13] Y. Yao, Z. Huang, P. Xie, S. D. Lacey, R. J. Jacob, H. Xie, F. Chen, A. Nie, T. Pu, M. Rehwoldt, D. Yu, M. R. Zachariah, C. Wang, Reza Shahbazian-Yassar , J. Li, L. Hu, *Science* **2018**, *359*, 1489-1494.
[14] J. Feng, D. Chen, P. V. Pikhitsa, Y.-h. Jung, J. Yang, M. Choi, *Matter* **2020**, *3*, 1646-1663.
[15] T. Löffler, A. Savan, A. Garzón-Manjón, M. Meischein, C. Scheu, A. Ludwig, W. Schuhmann, *ACS Energy Letters* **2019**, *4*, 1206-1214.
[16] S. S. Soliman, G. R. Dey, C. R. McCormick, R. E. Schaak, *ACS Nano* **2023**, *17*, 16147-16159.
[17] N. Zhou, S. Jiang, T. Huang, M. Qin, T. Hu, J. Luo, *Science Bulletin* **2019**, *64*, 856-864.
[18] M. Cui, C. Yang, B. Li, Q. Dong, M. Wu, S. Hwang, H. Xie, X. Wang, G. Wang, L. Hu, *Advanced Energy Materials* **2021**, *11*, 2002887.
[19] F. Li, Y. Ma, H. Wu, Q. Zhai, J. Zhao, H. Ji, S. Tang, X. Meng, *The Journal of Physical Chemistry C* **2022**, *126*, 18323-18332.
[20] A. Sarkar, L. Velasco, D. I. Wang, Q. Wang, G. Talasila, L. de Biasi, C. Kübel, T. Brezesinski, S. S. Bhattacharya, H. Hahn, B. Breitung, *Nature Communications* **2018**, *9*, 3400.
[21] G. R. Dey, S. S. Soliman, C. R. McCormick, C. H. Wood, R. R. Katzbaer, R. E. Schaak, *ACS Nanoscience Au* **2023**, *4*, 3-20.

[22] H. Wu, Z. Li, Z. Wang, Y. Ma, S. Huang, F. Ding, F. Li, Q. Zhai, Y. Ren, X. Zheng, Y. Yang, S. Tang, Y. Deng, X. Meng, *Applied Catalysis B: Environmental* **2023**, *325*, 122356.
[23] L. He, M. Li, L. Qiu, S. Geng, Y. Liu, F. Tian, M. Luo, H. Liu, Y. Yu, W. Yang, S. Guo, *Nature Communications* **2024**, *15*, 2290.
[24] L. Protesescu, S. Yakunin, M. I. Bodnarchuk, F. Krieg, R. Caputo, C. H. Hendon, R. X. Yang, A. Walsh, M. V. Kovalenko, *Nano Letters* **2015**, *15*, 3692-3696.
[25] Q. A. Akkerman, G. Rainò, M. V. Kovalenko, L. Manna, *Nature Materials* **2018**, *17*, 394-405.
[26] F. Liu, Y. Zhang, C. Ding, S. Kobayashi, T. Izuishi, N. Nakazawa, T. Toyoda, T. Ohta, S. Hayase, T. Minemoto, K. Yoshino, S. Dai, Q. Shen, *ACS Nano* **2017**, *11*, 10373-10383.
[27] Y. Wang, X. Li, J. Song, L. Xiao, H. Zeng, H. Sun, *Advanced Materials* **2015**, *27*, 7101-7108.
[28] Y. Lin, Y. Shao, J. Dai, T. Li, Y. Liu, X. Dai, X. Xiao, Y. Deng, A. Gruverman, X. C. Zeng, J. Huang, *Nature Communications* **2021**, *12*, 7.
[29] J. Yin, G. H. Ahmed, O. M. Bakr, J.-L. Brédas, O. F. Mohammed, *ACS Energy Letters* **2019**, *4*, 789-795.
[30] M. Imran, J. Ramade, F. Di Stasio, M. De Franco, J. Buha, S. Van Aert, L. Goldoni, S. Lauciello, M. Prato, I. Infante, S. Bals, L. Manna, *Chemistry of Materials* **2020**, *32*, 10641-10652.
[31] W. Van der Stam, J. J. Geuchies, T. Altantzis, K. H. W. Van Den Bos, J. D. Meeldijk, S. Van Aert, S. Bals, D. Vanmaekelbergh, C. de Mello Donega, *Journal of the American Chemical Society* **2017**, *139*, 4087-4097.
[32] Y. Zhou, Z. Zhou, M. Chen, Y. Zong, J. Huang, S. Pang, N. P. Padture, *Journal of Materials Chemistry A* **2016**, *4*, 17623-17635.
[33] M. Lu, X. Zhang, Y. Zhang, J. Guo, X. Shen, W. W. Yu, A. L. Rogach, *Advanced Materials* **2018**, *30*, 1804691.
[34] L. Xu, S. Yuan, H. Zeng, J. Song, *Materials Today Nano* **2019**, *6*, 100036.
[35] C. H. A. Li, P. Geng, S. B. Shivarudraiah, M. Ng, X. F. Zhang, B. Xu, L. Guo, J. E. Halpert, *Advanced Optical Materials* **2021**, *9*, 2100860.
[36] F. Brivio, K. T. Butler, A. Walsh, M. Van Schilfgaarde, *Physical Review B* **2014**, *89*, 155204.
[37] D. Weinberg, Y. Park, D. T. Limmer, E. Rabani, *Nano Letters* **2023**, *23*, 4997-5003.
[38] S. F. Solari, L.-N. Poon, M. Wörle, F. Krumeich, Y.-T. Li, Y.-C. Chiu, C.-J. Shih, *Journal of the American Chemical Society* **2022**, *144*, 2401048.
[39] L. Zhang, Y. Chen, Z. Zheng, Y. Zhou, C. Li, G. Li, B. Ren, Z. Hu, H. Zhou, F. Ren, *Advanced Functional Materials* **2025**, 2423450.
[40] J. Guo, Y. Fu, W. Zheng, M. Xie, Y. Huang, Z. Miao, C. Han, W. Yin, J. Zhang, X. Yang, J. Tian, X. Zhang, *Nano Letters* **2023**, *24*, 417-423.
[41] J. Song, J. Li, L. Xu, J. Li, F. Zhang, B. Han, Q. Shan, H. Zeng, *Advanced Materials* **2018**, *30*, 1800764.
[42] N. Phung, R. Félix, D. Meggiolaro, A. Al-Ashouri, G. Sousa e Silva, C. Hartmann, J. Hidalgo, H. Köbler, E. Mosconi, B. Lai, R. Gunder, M. Li, L. Wang, Z.-K. Wang, K. Nie, E. Handick , R. G. Wilks , J. A. Marquez, B. Rech, T. Unold, J.-P. Correa-Baena, S. Albrecht, F. De Angelis, M. Bär, A. Abate, *Journal of the American Chemical Society* **2020**, *142*, 2364-2374.
[43] B. Luo, F. Li, K. Xu, Y. Guo, Y. Liu, Z. Xia, J. Z. Zhang, *Journal of Materials Chemistry C* **2019**, *7*, 2781-2808.
[44] M. C. Folgueras, Y. Jiang, J. Jin, P. Yang, *Nature* **2023**, *621*, 282-288.
[45] J. Butkus, P. Vashishtha, K. Chen, J. K. Gallaher, S. K. K. Prasad, D. Z. Metin, G. Laufersky, N. Gaston, J. E. Halpert, J. M. Hodgkiss, *Chemistry of Materials* **2017**, *29*, 3644-3652.
[46] X. Ma, H. Gao, C. Meng, F. Pan, H. Ye, *The Journal of Physical Chemistry Letters* **2023**, *14*, 6860-6866.
[47] H. Zhao, G. Liu, S. You, F. V. A. Camargo, M. Zavelani-Rossi, X. Wang, C. Sun, B. Liu, Y. Zhang, G. Han, A. Vomiero, X. Gong, *Energy & Environmental Science* **2021**, *14*, 396-406.
[48] H. Gogoi, S. S. Pathak, S. Dasgupta, L. S. Panchakarla, S. Nath, A. Datta, *The Journal of Physical Chemistry Letters* **2022**, *13*, 6770-6776.
[49] S. C. Boehme, M. I. Bodnarchuk, M. Burian, F. Bertolotti, I. Cherniukh, C. Bernasconi, C. Zhu, R. Erni, H. Amenitsch, D. Naumenko, H. Andrusiv, N. Semkiv, R. Abraham John, A. Baldwin, K. Galkowski, N. Masciocchi, S. D. Stranks, G. Rainò, A. Guagliardi, M. V. Kovalenko, *ACS nano* **2023**, *17*, 2089-2100.
[50] S. Bera, D. Ghosh, A. Dutta, S. Bhattacharyya, S. Chakraborty, N. Pradhan, *ACS Energy Letters* **2019**, *4*, 1364-1369.
[51] S. Yuan, Z.-K. Wang, M.-P. Zhuo, Q.-S. Tian, Y. Jin, L.-S. Liao, *ACS Nano* **2018**, *12*, 9541-9548.
[52] J. Jagielski, S. Kumar, M. Wang, D. Scullion, R. Lawrence, Y.-T. Li, S. Yakunin, T. Tian, M. V. Kovalenko, Y.-C. Chiu, E. J. G. SANTOS, S. LIN, C.-J. SHIH, *Science Advances* **2017**, *3*, eaaq0208.
[53] J. Ye, M. M. Byranvand, C. O. Martínez, R. L. Z. Hoye, M. Saliba, L. Polavarapu, *Angewandte Chemie* **2021**, *133*, 21804-21828.
[54] Q. Zhang, B. Wang, W. Zheng, L. Kong, Q. Wan, C. Zhang, Z. Li, X. Cao, M. Liu, L. Li, *Nature Communications* **2020**, *11*, 31.
[55] A. De, N. Mondal, A. Samanta, *Nanoscale* **2017**, *9*, 16722-16727.
[56] W. Zhao, D. Yang, Z. Yang, S. F. Liu, *Materials Today Energy* **2017**, *5*, 205-213.
[57] C. Chen, T. Xuan, W. Bai, T. Zhou, F. Huang, A. Xie, L. Wang, R.-J. Xie, *Nano Energy* **2021**, *85*, 106033.
[58] W. Shen, J. Zhang, R. Dong, Y. Chen, L. Yang, S. Chen, Z. Su, Y. Dai, K. Cao, L. Liu, S. CHEN, W. HUANG, *Research* **2021**.
[59] B. T. Diroll, G. Nedelcu, M. V. Kovalenko, R. D. Schaller, *Advanced Functional Materials* **2017**, *27*, 1606750.
[60] A. Dey, P. Rathod, D. Kabra, *Advanced Optical Materials* **2018**, *6*, 1800109.
[61] X. Li, Y. Wu, S. Zhang, B. Cai, Y. Gu, J. Song, H. Zeng, *Advanced Functional Materials* **2016**, *26*, 2435-2445.
[62] G. Ghosh, B. Jana, S. Sain, A. Ghosh, A. Patra, *Physical Chemistry Chemical Physics* **2019**, *21*, 19318-19326.
[63] Z. Yang, X. Yuan, Y. Song, M. Chen, K. Xing, S. Cao, J. Zheng, J. Zhao, *The Journal of Physical Chemistry C* **2023**, *127*, 21227-21234.
[64] S. Ji, X. Yuan, J. Li, J. Hua, Y. Wang, R. Zeng, H. Li, J. Zhao, *The Journal of Physical Chemistry C* **2018**, *122*, 23217-23223.
[65] R. Chakraborty, A. Nag, *The Journal of Physical Chemistry C* **2020**, *124*, 16177-16185.
[66] S. Rana, K. Awasthi, S. S. Bhosale, E. W.-G. Diau, N. Ohta, *The Journal of Physical Chemistry C* **2019**, *123*, 19927-19937.
[67] K. Zheng, Q. Zhu, M. Abdellah, M. E. Messing, W. Zhang, A. Generalov, Y. Niu, L. Ribaud, S. E. Canton, T. Pullerits, *The journal of physical chemistry letters* **2015**, *6*, 2969-2975.
[68] A. Shinde, R. Gahlaut, S. Mahamuni, *The Journal of Physical Chemistry C* **2017**, *121*, 14872-14878.
[69] M. Li, P. Huang, H. Zhong, *The Journal of Physical Chemistry Letters* **2023**, *14*, 1592-1603.
[70] M. Gramlich, M. W. Swift, C. Lampe, J. L. Lyons, M. Döblinger, A. L. Efros, P. C. Sercel, A. S. Urban, *Advanced Science* **2022**, *9*, 2103013.
[71] A. D. Wright, C. Verdi, R. L. Milot, G. E. Eperon, M. A. Pérez-Osorio, H. J. Snaith, F. Giustino, M. B. Johnston, L. M. Herz, *Nature Communications* **2016**, *7*, 11755.
[72] K. Abiedh, Z. Zaaboub, F. Hassen, *Applied Physics A* **2021**, *127*, 1-9.
[73] Y. Gao, C. S. S. Sandeep, J. M. Schins, A. J. Houtepen, L. D. A. Siebbeles, *Nature Communications* **2013**, *4*, 2329.
[74] G. M. Akselrod, F. Prins, L. V. Poulikakos, E. M. Y. Lee, M. C. Weidman, A. J. Mork, A. P. Willard, V. Bulović, W. A. Tisdale, *Nano letters* **2014**, *14*, 3556-3562.

[75] N. Yarita, H. Tahara, T. Ihara, T. Kawawaki, R. Sato, M. Saruyama, T. Teranishi, Y. Kanemitsu, *The journal of physical chemistry letters* **2017**, *8*, 1413-1418.
[76] N. Mondal, A. De, S. Das, S. Paul, A. Samanta, *Nanoscale* **2019**, *11*, 9796-9818.
[77] S. Nakahara, H. Tahara, G. Yumoto, T. Kawawaki, M. Saruyama, R. Sato, T. Teranishi, Y. Kanemitsu, *The Journal of Physical Chemistry C* **2018**, *122*, 22188-22193.
[78] A. Zunger, S. H. Wei, L. G. Ferreira, J. E. Bernard, *Physical review letters* **1990**, *65*, 353.
[79] J. Kang, L.-W. Wang, *The Journal of Physical Chemistry Letters* **2017**, *8*, 489-493.
[80] M. A. Becker, R. Vaxenburg, G. Nedelcu, P. C. Sercel, A. Shabaev, M. J. Mehl, J. G. Michopoulos, S. G. Lambrakos, N. Bernstein, J. L. Lyons, T. Stöferle, R. F. Mahrt, M. V. Kovalenko, D. J. Norris, G. Rainò, A. L. Efros, *Nature* **2018**, *553*, 189-193.
[81] S. Feldmann, M. K. Gangishetty, I. Bravić, T. Neumann, B. Peng, T. Winkler, R. H. Friend, B. Monserrat, D. N. Congreve, F. Deschler, *Journal of the American Chemical Society* **2021**, *143*, 8647-8653.
[82] G. H. Ahmed, Y. Liu, I. Bravić, X. Ng, I. Heckelmann, P. Narayanan, M. S. Fernández, B. Monserrat, D. N. Congreve, S. Feldmann, *Journal of the American Chemical Society* **2022**, *144*, 15862-15870.
[83] A. A. Bol, A. Meijerink, *Physical Review B* **1998**, *58*, R15997.
[84] D. Wu, K. Kusada, Y. Nanba, M. Koyama, T. Yamamoto, T. Toriyama, S. Matsumura, O. Seo, I. Gueye, J. Kim, L. S. Rosantha Kumara , O. Sakata , S. Kawaguchi , Y. Kubota , H. Kitagawa *Journal of the American Chemical Society* **2022**, *144*, 3365-3369.
[85] S. Siol, J. Mann, J. Newman, T. Miyayama, K. Watanabe, P. Schmutz, C. Cancellieri, L. P. H. Jeurgens, *Surface and Interface Analysis* **2020**, *52*, 802-810.
[86] G. Greczynski, L. Hultman, *Scientific Reports* **2021**, *11*, 11195.
[87] A. Wieczorek, H. Lai, J. Pious, F. Fu, S. Siol, *Advanced Materials Interfaces* **2023**, *10*, 2201828.
[88] D. N. Dirin, A. Vivani, M. Zacharias, T. V. Sekh, I. Cherniukh, S. Yakunin, F. Bertolotti, M. Aebli, R. D. Schaller, A. Wieczorek, *Nano letters* **2023**, *23*, 1914-1923.
[89] S. Zhuk, A. Wieczorek, A. Sharma, J. Patidar, K. Thorwarth, J. Michler, S. Siol, *Chemistry of Materials* **2023**, *35*, 7069-7078.
[90] Y. Li, D. Wang, Y. Yang, C. Ding, Y. Hu, F. Liu, Y. Wei, D. Liu, H. Li, G. Shi, S. Chen, H. Li, A. Fuchimoto , K. Tosa , U. Hiroki, S. Hayase, H. Wei , Q. Shen, *Journal of the American Chemical Society* **2024**, *146*, 3094-3101.
[91] S. F. Solari, A. Wieczorek, T. Marcato, M. Wörle, F. Krumeich, Y. T. Li, Y. C. Chiu, S. Siol, S. B. Shivarudraiah, C. J. Shih, *Advanced Optical Materials*, *144*, 2401048.
[92] S. Wang, A. A. Yousefi Amin, L. Wu, M. Cao, Q. Zhang, T. Ameri, *Small Structures* **2021**, *2*, 2000124.
[93] H. Huang, M. I. Bodnarchuk, S. V. Kershaw, M. V. Kovalenko, A. L. Rogach, *ACS Energy Letters* **2017**, *2*, 2071-2083.
[94] A. Wieczorek, A. G. Kuba, J. Sommerhäuser, L. N. Caceres, C. M. Wolff, S. Siol, *Journal of Materials Chemistry A* **2024**, *12*, 7025-7035.
[95] R. D. Shannon, *Foundations of Crystallography* **1976**, *32*, 751-767.
[96] V. M. Goldschmidt, *Naturwissenschaften* **1926**, *14*, 477-485.